19. Fendley, P. & Saleur, H. Nonequilibrium dc noise in a Luttinger liquid with an impurity. *Phys. Rev. B* **54,** 10845–10854 (1996).
20. Martin, Th & Landauer, R. Wave packet approach to noise in multichannel mesoscopic systems. *Phys. Rev. B* **45,** 1742–1755 (1992).

Acknowledgements. We thank G. Bunin for manufacturing the transistors for the cooled preamplifier, and D. Mahalu for performing the e-beam lithography. This work was partly supported by the Israeli Science Foundation, the German-Israeli Foundation and the Israeli Ministry of Science.

Correspondence and requests for materials should be addressed to M.H. (e-mail: heiblum@wis.weizmann.ac.il)

Two types of avalanche behaviour in granular media

Adrian Daerr & Stéphane Douady

Laboratoire de Physique Statistique de l'ENS, 24 rue Lhomond, 75231 Paris CEDEX 05, France

The nature of the transition between static and flowing regimes in granular media[1,2] provides a key to understanding their dynamics. When a pile of sand starts flowing, avalanches occur on its inclined free surface. Previously, studies[3] of avalanches in granular media have considered the time series of avalanches in rotating drums[4], or in piles continuously fed with material. Here we investigate single avalanches created by perturbing a static layer of glass beads on a rough inclined plane. We observe two distinct types of avalanche, with evidence for different underlying physical mechanisms. Perturbing a thin layer results in an avalanche propagating downhill and also laterally owing to collisions between neighbouring grains, causing triangular tracks; perturbing a thick layer results in an avalanche front that also propagates upwards, grains located uphill progressively tumbling down because of loss of support. The perturbation threshold for triggering an avalanche is found to decrease to zero at a critical slope. Our results may improve understanding of naturally occurring avalanches on snow slopes[5] where triangular tracks are also observed.

The experiments are done on an inclined plane covered with velvet cloth. This surface is chosen so that the glass beads (180–300 μm in diameter), our granular material, have a larger friction with it than between themselves. A thin layer of grains can thus remain static on the plane up to a larger angle than if it were on a grain pile. We set the plane to an angle φ (larger than the pile angle φ_0) and pour glass beads abundantly at the top. The moving beads leave behind a static layer of uniform thickness $h(\varphi)$ (arrow leading to point a in Fig. 1; the geometry of the system is shown in Fig. 1 inset). This effect is explained by the variation of the friction of the successive grain layers with their distance to the surface of the inclined slope[6]: it is maximum for the bottom layer, and decreases continuously to the value for a thick pile. The top static layer is that which has a large enough friction coefficient on the underlying layers $\mu(h)$ to come to a stop. At inclination angle φ, the friction coefficient of this top static layer is then $\mu(h) = \tan\varphi$. The measurements $h(\varphi)$ of Fig. 1 thus give the variation of the coefficient of friction with depth[7]. We obtain a simple exponential decay as in ref. 7:

$$\mu(h) = \mu(\infty) + \Delta\mu[\exp(-h/h_0)] \qquad (1)$$

with h_0 of the order of $2d$, where $d = 240$ μm is taken as the mean diameter of the grains, and $\Delta\mu = \mu(0) - \mu(\infty)$ is the difference between the friction coefficient at the plane and that in the pile.

This remaining static layer is dynamically stable. If we add some beads onto this layer, they move downwards like a drop of liquid, leaving the layer unaffected. We can even jolt the experiment sharply: the whole layer starts to move but 'freezes' again very quickly.

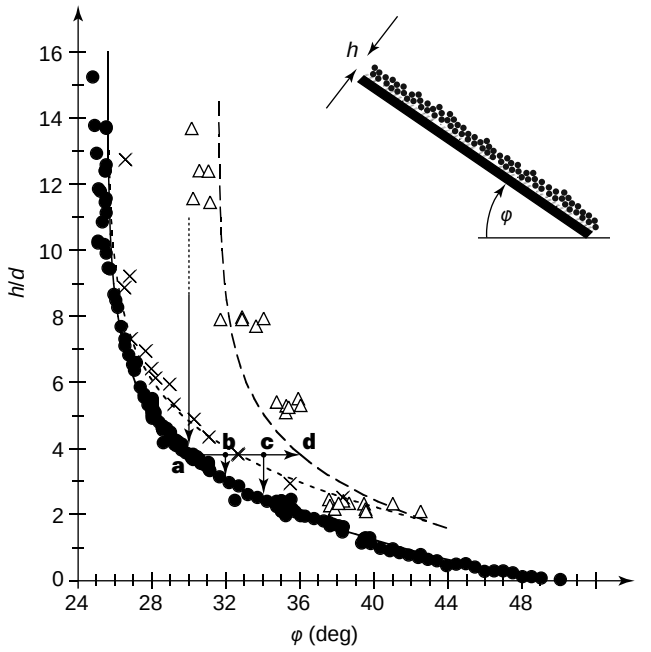

Figure 1 Stability diagram. Inset, the geometry of the experiment. Main figure, plot of h/d versus φ. The arrows sketch the course of an experiment. The filled circles show the measured thickness h of the layer left after a massive avalanche over the plane set at an angle φ (point a). The solid line is a fit according to equation (1). When these static layers are tilted they start flowing spontaneously at angles given by the open triangles (point d). The long-dashed line indicates the stability limit of a static layer. The hysteretic region between the solid and the long-dashed line is separated by the crosses (and the short-dashed line). Below them (for example, point b) a finite disturbance will generate a triangular avalanche. Above them (for example, point c) it will result in an avalanche front which also propagates uphill. For preparation angles φ >34°, we observed only triangular avalanches (even the spontaneous ones). The precision of the measurements is smaller than the point size, and negligible compared to the physical fluctuations.

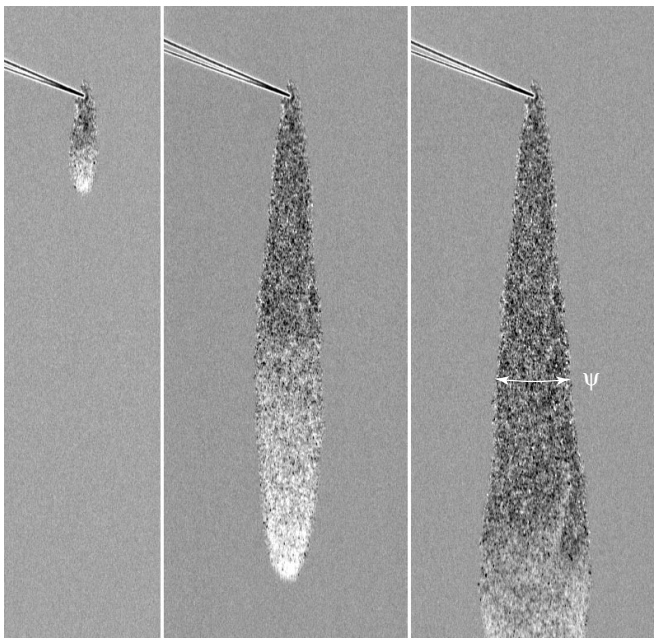

Figure 2 Evolution of a triangular avalanche ($\varphi = 30°$, $\delta\varphi = 1.5°$), showing the opening angle ψ. The time lapse between two images is 3.04 s. The pointed object is a pin used to trigger the avalanche, and indicates the origin of the avalanche.

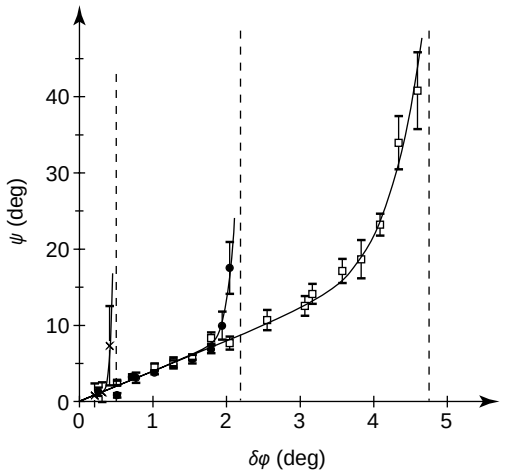

Figure 3 Opening angle ψ of triangular avalanches, as a function of the additional tilt $\delta\varphi$. The three sets of points correspond to $\varphi = 25°$ (crosses), 28° (circles) and 32.5° (squares). For $\delta\varphi = 0$, we observe a drop, or a non-growing avalanche ($\psi = 0$). As $\delta\varphi$ increases, the opening angle first grows linearly, with a slope independent of φ. Just before the transition to the uphill propagation regime, (dashed lines, $\varphi = 0.5°$, 2.25° and 4.75°, respectively), there is a sharp increase of ψ.

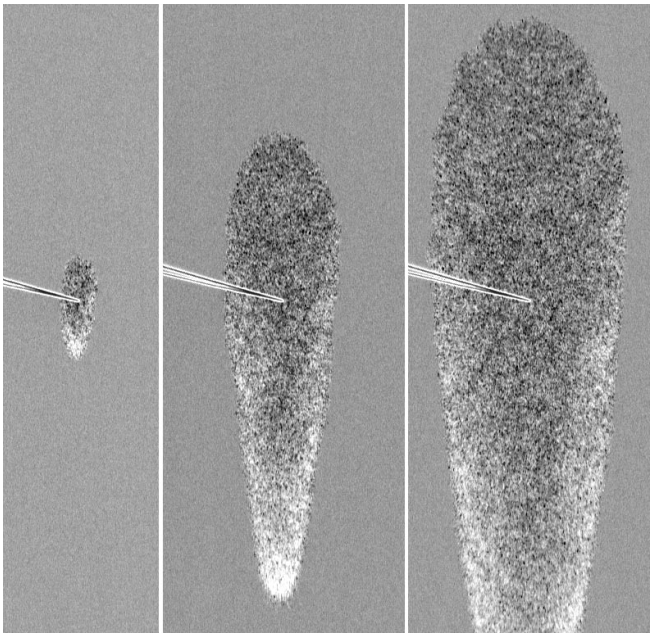

Figure 4 Three photographs of an uphill-propagating avalanche ($\varphi = 30°$, $\delta\varphi = 2.5°$). The point of the pin indicates where the avalanche was triggered: the time lapse between two images is 1.52 s. The upper front of the avalanche is now rounded, like a front propagating with different upward and sideward velocities. The uphill velocity jumps from zero to ~5 cm s^{-1} at the threshold, and then increases roughly linearly to 20 cm s^{-1} with increasing $\delta\varphi$. In the same interval, the velocity of the lower front increases linearly from 10 to 30 cm s^{-1}.

We then increase the tilting angle of the plane to $\varphi + \delta\varphi$ (from point a to point b in Fig. 1). For a small value of $\delta\varphi$, the layer remains perfectly static. But if we create a finite-sized disturbance (by setting some beads into motion or by pouring additional ones), an avalanche occurs. The height of the layer which is left behind an avalanche, $h(\varphi + \delta\varphi)$, is smaller than the initial height (Fig. 1). The avalanche, while running down, thus collects new material and becomes larger. Depending on both φ and $\delta\varphi$, we observe two types of propagation for the avalanches.

In the first type, for small $\delta\varphi$ or for thin layers (below the short-dashed line of Fig. 1, for example, point b), the avalanches grow laterally on their way down, leaving tracks of triangular shape. Figure 2 shows three successive pictures of such a 'triangular avalanche'. Although the total moving mass is increasing rapidly with time, the moving front reaches a constant velocity and thickness, the added rolling grains being spread behind the front (see Fig. 2). The lateral propagation is due only to a small number of grains which drive into motion some of their lateral neighbours. This process repeats, producing straight edges. The opening angle ψ of the resulting triangles (Fig. 2) increases at first proportionally to $\delta\psi$ (Fig. 3).

The second type of avalanche is obtained for large $\delta\varphi$ or for thick layers (above the short-dashed line of Fig. 1, for example, point c). In this case, the avalanche front propagates upwards; that is, the grains located uphill start to tumble down spontaneously due to the loss of their support. Contrary to the previous case, the whole layer will eventually flow. Figure 4 shows three successive pictures of such an uphill-propagating perturbation.

If we keep tilting the plane without doing any perturbation, the grain layer remains static up to a limiting value $\delta\varphi_s$ (point d in Fig. 1), where avalanches occur spontaneously. The angle hysteresis does not seem to depend much on the depth of the layer[6], so the long-dashed line drawn in Fig. 1 has been chosen as the translation of $h(\varphi)$ by 6° as in ref. 6. The larger fluctuation observed here compared to ref. 6 could be due to the elasticity and roughness being larger for the material used here for the surface of the inclined plane (velvet) than that used in ref. 6 (glued beads).

To investigate this hysteresis between the static and dynamical angles, we did the following experiment: we pour a few grains very gently onto the surface of the layer, and record the minimum quantity of grains that is required, at a given $\delta\varphi$, to trigger an avalanche. The result (Fig. 5) shows a clear signature of a subcritical bifurcation: close to the initial slope φ, a considerable added height (of more than twice the layer thickness) is needed to get an avalanche (or a drop for $\delta\varphi = 0$) started. Less and less perturbation is needed as $\delta\varphi$ increases, until finally, it can become as small as one grain.

We note that the tilt angle for which only one grain starts an avalanche is smaller than the one for which a spontaneous avalanche occurs. This comes from the fact that the falling grain is already in motion, while observations show that spontaneous avalanches occur when a previously motionless grain spontaneously rolls down. This sensitivity to the stability of one surface grain is the source of the large dispersion measured for the static limit (Fig. 1) when the experiment is repeated: the surface has a fluctuating roughness, with some grains more unstable than others.

The transition from lateral and downhill propagation to uphill propagation could at first be interpreted as the point where the opening angle of triangular avalanches exceeds 180° (similar to the subsonic/supersonic transition or convective/absolute instability). But measuring $\psi(\delta\varphi)$ for several φ (Fig. 3) showed that triangular avalanches close to the threshold for upward motion still have small opening angles. The transition to upward propagation is not linked either to any particular value of $\delta\varphi$: the threshold on $\delta\varphi$ for upward propagation increases with φ. But inside the triangular avalanche domain, in contrast, the $\psi(\delta\varphi)$ curves for different φ can be superposed, which means that there is no dependence on φ. These observations indicate that the physical mechanisms underlying the lateral propagation of the triangular avalanches are

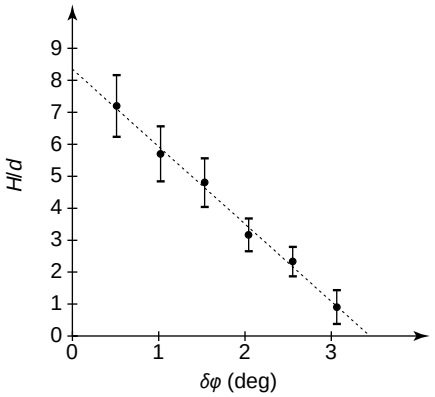

Figure 5 Avalanche threshold. The initial angle is $\varphi = 32°$; the height of the minimum perturbation triggering an avalanche is plotted as a function of the additional tilt $\delta\varphi$. We use an inclined tube to release from a very small height additional glass beads practically one by one at one spot on the surface[8]. As soon as an avalanche has occurred, the delivery is stopped and the added mass m is measured. We calculate an equivalent added height $H = [(3/\pi)[\tan^2(\beta)]m/\rho]^{1/3}$ as the beads form a cone of slope $\beta \approx 30°$ and mean density $\rho = 1.48\ g\ cm^{-3}$ on top of the existing layer. This height decreases roughly linearly with $\delta\varphi$, as indicated by the short-dashed line. The error bars are the statistical error over ten measurements.

different in nature from those for upward propagation.

Careful observation of the motions of grains shows that these reach their limiting velocity very rapidly and go straight down the slope. The lateral spread of the triangular avalanches can thus be interpreted as due to the friction exerted by the rolling grains on their lateral neighbours being sufficient to set some of them into motion. On the other hand, in upward propagation, the grains start to roll down spontaneously because the grains located below them are already gone. The threshold of this uphill motion is compatible with the condition that the thickness difference between the initial layer and the new static layer is larger than a typical height, taken as one particle diameter for the short-dashed line in Fig. 1.

We observed the same two types of behaviour with other materials (crushed walnut shells and Sinai sand). We can thus think of comparing these avalanches with other types of avalanche (of snow or rocks) occurring in a geological context. In these cases, the triggering, amplification and velocity of the avalanches are of practical importance. Comparisons can already be made with some snow avalanches, where triangular tracks are observed at their origin[5]. In our experiment we have observed triangular avalanches exclusively in the case where a thin layer is located over a surface creating a strong friction. In all the other cases, the avalanche front propagates uphill. This suggests that the variation of friction coefficient across the layer also plays an important role in snow avalanches. □

Received 30 November 1998; accepted 11 March 1999.

1. Reynolds, O. On the dilatancy of media composed of rigid particles in contact. *Phil. Mag.* **20,** 469–481 (1885).
2. Bagnolds, R. A. The shearing and dilatation of dry sand and the 'singing' mechanism. *Proc. R. Soc. Lond. A* **295,** 219–232 (1966).
3. Rajchenbach, J. in *Physics of Dry Granular Media* (eds Hermann H., Hovi, J.-P. & Luding, S.) 421–440 (Kluwer, Dordrecht, 1998).
4. Caponieri, M., Douady, S., Fauve, S. & Laroche, C. in *Mobile Particulate Systems* (eds Guazzelli, E. & Oger, L.) 331–366 (Kluwer, Dordrecht, 1995).
5. McClung, D. *Avalanche Handbook* (Mountaineers, Seattle, 1993).
6. Pouliquen, O. & Renaut, N. Onset of granular flows on an inclined rough surface: dilatancy effects. *J. Phys. II France* **6,** 923–935 (1996).
7. Pouliquen, O. Scaling laws in granular flows down rough inclined planes. *Phys. Fluids* (in the press).
8. Held, G. A. *et al.* Experimental study of critical-mass fluctuations in an evolving sandpile. *Phys. Rev. Lett.* **65,** 1120–1123 (1990).

Acknowledgements. This work was supported by the University Paris VII through BQR97.

Correspondence and requests for materials should be addressed to A.D. (e-mail: daerr@physique.ens.fr).

Desorption–ionization mass spectrometry on porous silicon

Jing Wei*, Jillian M. Buriak† & Gary Siuzdak*

* *Departments of Molecular Biology and Chemistry, The Scripps Research Institute, BCC157, 10550 North Torrey Pines Road, La Jolla, California 92037, USA*

† *Department of Chemistry, Purdue University, West Lafayette, Indiana 47907-1393, USA*

Desorption mass spectrometry has undergone significant improvements since the original experiments were performed more than 90 years ago[1]. The most dramatic change occurred in the early 1980s with the introduction of an organic matrix[2–4] to transfer energy to the analyte. This reduces ion fragmentation but also introduces background ions from the matrix. Here we describe a matrix-free strategy for biomolecular mass spectrometry based on pulsed-laser desorption–ionization from a porous silicon[5] surface. Our method uses porous silicon to trap analytes deposited on the surface, and laser irradiation to vaporize and ionize them. We show that the method works at femtomole and attomole levels of analyte, and induces little or no fragmentation, in contrast to what is typically observed with other such approaches[6–11]. The ability to perform these measurements without a matrix[3,4,12,13] also makes it more amenable to small-molecule analysis. Chemical[14] and structural[15] modification of the porous silicon has enabled optimization of the ionization characteristics of the surface. Our technique offers good sensitivity as well as compatibility with silicon-based microfluidics and microchip technologies.

The broad success of matrix-assisted desorption/ionization is related to the ability of the matrix to incorporate and transfer energy to the analyte[3,4,12,16]. For instance, in matrix-assisted laser desorption/ionization (MALDI)[4], the analyte is typically dissolved into a solid ultraviolet-absorbing organic acid matrix which vaporizes upon pulsed-laser radiation, carrying with it the analyte[16]. Direct desorption/ionization without matrix has been extensively studied on a variety of surfaces[6–11] but has not been widely used because of the rapid molecular degradation that is usually observed upon direct exposure to laser radiation. However, just as secondary ion mass spectrometry (SIMS) has had a profound effect on surface science[17], the utility of direct laser desorption/ionization for biomolecular analysis could be highly beneficial owing to dramatically simplified sample preparation, elimination of matrix background ions, and other advantages we describe here.

Our matrix-free desorption approach uses the porous silicon surface to trap the analyte molecules and, because of its high absorptivity in the ultraviolet[18], act as an energy receptacle for the laser radiation. The experimental protocol for desorption/ionization on silicon (DIOS) (see Methods and Fig. 1) involves the generation of porous silicon from flat crystalline silicon by using a simple galvanostatic etching procedure[15]. A micrometres-thick porous layer with a nanocrystalline architecture is produced that exhibits bright photoluminescence upon exposure to ultraviolet light[5,19]. The thickness, morphology, porosity, resistivity and other characteristics of the material are readily modulated through the choice of silicon-wafer precursor and etching conditions (see Methods). Freshly etched porous silicon surfaces are hydrophobic owing to the metastable, silicon-hydride termination, but through Lewis-acid-mediated[14] or light-promoted hydrosilylation reactions[20], the surface can be easily stabilized and functionalized as required. Because of the high stability of the hydrophobic, hydrosilylated surfaces to aqueous media, these surfaces can be reused repeatedly (see Methods) with little degradation[14,20]. Photopatterning of the